Damage advancement behavior in braided composite structure for mini aerial vehicle

Yucheng Zhong[a, b], Ravindrababu Suraj[a], Chen Wang[c], Elvin Ser Ming Chia[d], Sunil Chandrakant Joshi[e*], Zhong Chen[c*]

[a] Temasek Laboratories @ NTU, Nanyang Technological University, Singapore 637553
[b] School of Science, Wuhan University of Technology, 122 Luoshi Road, Wuhan, China
[c] School of Materials Science and Engineering, Nanyang Technological University, Singapore 639798
[d] DSO National Laboratories, 20 Science Park Drive, Singapore 118230
[e] School of Mechanical and Aerospace Engineering, Nanyang Technological University, Singapore 639798

Abstract

This work provides a systematic approach to accurately predict damage progression in a composite structure subjected to bending load. Landing gear structures for unmanned aerial vehicle (UAV) were fabricated from braided textile preforms and assessed for flexural behavior. A multi-scale finite element analysis (FEA) model was developed for analyzing the progressive damage of these structures under bending loads. Micro-scale and meso-scale analyses were carried out first. Subsequently, the results of micro-scale and meso-scale analyses were used as inputs in macro-scale analyses that predicted the progressive damages in the entire landing gear structure. The numerical results were validated by experimental studies.

Keywords braided composite, landing gear, bending, finite element, multi-scale, progressive damage

1. Introduction

Braiding is a type of textile process [1], where a number of rolls of fiber yarns are fed to a mandrel by a braiding machine to obtain dry fiber braids. The braiding angle of the fiber braids (orientation of fibers) is controlled by the number of fiber rolls, the diameter of the mandrel, etc. Later, these dry fiber braids are impregnated by resins through processes such as vacuum assisted resin transfer molding to make composite parts. This manufacturing technique offers high production rate and is particularly suited for hollow structures such as tubes. It also provides flexibility in terms of design of the properties of composites by altering the braiding angle. It allows through-the-thickness strengthening by introducing 3D braided fiber preforms.

* Corresponding Author. Sunil Chandrakant Joshi: Tel. (+65) 6790 5170; Email MSCJOSHI@ntu.edu.sg;
Zhong Chen: Tel. (+65) 6790 4256; Email ASZChen@ntu.edu.sg.

Advantages of braided textile composites include but not limited to increased transverse moduli and strength [2], improved shear resistance [3], fracture toughness [4] and damage tolerance [5]. Moreover, braided composites are well suited for complex shapes [6].

The complicated architectures of reinforcing fibers in braided composites add to the difficulty in predicting their mechanical behavior. Good numerical and analytical prediction techniques suitable for braided textile composites are yet to be developed to attend to the needs of practical applications [7-9]. Numerical and analytical models for different structures, including braided tubes [10], surface-core braided structures [11], 2D and 3D braided composites [12-13], and for different loading conditions, e.g., tension [14], compression [15], crush [16], etc., have been reported so far. However, relevant models for braided composites are still relatively limited. Limited access to braided fiber preforms with the desired geometry and difficulty in the construction of the representative volume elements partially explain such scarcity.

The initiation and propagation of damage plays a key role for the successful prediction of damage and strength of composite structures during the course of finite element analysis. Different finite element solvers usually have their own mechanisms of failure detection. For instance, the Hashin criteria [17] are available in ABAQUS Standard/Explicit solver. Madukauwa-David and Drissi-Habti [18] simulated the mechanical behavior of a large composite platform under three-point bending load. The Hashin criteria were selected for their ease of use within the ABAQUS environment, and the possibility of examining fiber and matrix, tensile and compressive damage separately. However, failure criteria or damage initiation mechanism available in these solvers are limited. The flexibility in implementing failure criteria which comprehensively account for potential failure modes and are more suitable for certain cases is desired for finite element analysis. The UMAT (or VUMAT for ABAQUS/ Explicit) and

USDFLD user interface available in ABAQUS caters for such need. The constitutive models available in ABAQUS solver are insufficient in certain cases to accurately account for the behavior of structural materials. The UMAT user interface allows engineers to define their own constitutive models. Dai and Cunningham [19] programmed a VUMAT code to calculate the deformation in 3D woven composites while Panamoottil et al. [20] developed an anisotropic strain-dependent material damage model and implemented it in the finite element program ABAQUS via UMAT interface. Wang et al. [21] proposed a multi-scale approach for the prediction of the progressive damage in braided composites in which USDFLD user subroutine was used to calculate failure indices.

The objective of this investigation is to develop a numerical model for the prediction of the mechanical response of a landing gear structure under flexure, which involves both tensile and compressive stresses. The face-sheet of the sandwich structure was bi-axially braided textile composites. Based on the architectures of the fiber tows in the braided composites, a multi-scale approach was decided (i.e., micro-scale, meso-scale and macro-scale) for the progressive damage analysis of the landing gear structure. The simulation work was carried out using the commercial finite element software, ABAQUS (v.6.14). At each scale of analysis, USDFLD user subroutine involving relevant failure criteria as well as field variables were coded to identify possible failures inside the structure or elements. In the meantime, a degradation scheme was carried out at each iteration which recalculated the elastic constants of the constituents based on stress analysis. The outcome of FEA analysis was compared with experimental observations.

2. Experiments

2.1 Materials and sample fabrication

The face-sheets of the landing gear were bi-axial carbon fiber braids reinforced epoxy composites while the core was PU 4507 foam core, which was a type of polyurethane foam. The

fiber in the composite face-sheets was A-42 carbon fiber while the matrix was L20 epoxy resin. The hardener was EPH-960. The raw materials for the PU foam were mixed and manually stirred. Later, the mixture was poured into an aluminum mold. The poured mixture would expand and fill the cavity of the mold to form the desired shape. The foam core thus prepared is shown in Figure 1a. In the meantime, carbon fiber sleeves were fabricated using a braiding machine (Figure 2). The foam core was then wrapped into two A-42 carbon fiber sleeves by manually pulling them over (Figure 1b). The landing gear assembly (foam core and A-42 carbon fiber sleeves) was placed into an aluminum mold. A vacuum bag was prepared (Figure 1c) and the landing gear was fabricated through a vacuum assisted resin infusion process. The landing gear was cured at room temperature for 72 hours. Later, it was taken out from the aluminum mold and subjected to post curing at 80ºC for 4 hours. The final structure obtained is shown in Figure 1d. The thickness of the face sheet is 1.5 mm. The thickness of the foam core at the center is 10 mm, giving a total thickness of 13 mm at the center of the landing gear. The fiber volume fraction in the face-sheet of the cured landing gear was measured to be 63.6%.

2.2 Testing

Two landing gears consisting of face sheets of braided textile composites and PU foam core were fabricated and tested under bending load. An aluminum supporting rail (Figure 3) was designed for the bending test of the landing gear. The landing gear was supported by Teflon wheels at both ends (Figure 3b), which were able to move freely on the supporting rail. Therefore, both ends of the landing gear were able to move freely. The testing speed (speed of the loading roller) during testing was 1mm/min. The diameter of the loading roller was 10 mm. The testing results are summarized in Table 1. The average peak flexure load measured during experiments was 891.6N.

3. Details of multi-scale approach

The bi-axially braided composites of the face-sheet of the landing gear consisted of fiber yarns of certain braiding angles (i.e., ±θ) and matrix resin. Different sections of the landing gear had different widths and different braiding angles. The braiding angles of different sections of the composite face-sheet are shown in Figure 4. Based on the unique architecture of its microstructure, a multi-scale approach was developed to simulate the mechanical behavior of the landing gear. The flowchart of the multi-scale approach is summarized in Figure 5. Micro-scale analyses were performed first to calculate the properties of fiber yarn. The properties of the fiber yarn was then treated as inputs for the meso-scale analyses which aimed to obtain the homogenized properties for the composite face-sheet of the landing gear.

Progressive damage analyses were carried out during micro-scale, meso-scale and macro-scale analyses which identified failures and constructed updated stiffness matrices of the constituents. The process of typical progressive damage analysis is illustrated in Figure 6. The ABAQUS solver worked in connection with USDFLD user subroutines which were coded in Fortran 77 programming language. Failure criteria based on specific failure modes were included in the USDFLD user subroutine which defined the failure occurred to the elements. Once a failure was detected, the material property would be degraded according to the specific failure modes. If failure in fiber direction occurred, all the elastic constants of the material would be reduced to 1%.

3.1 Micro-scale analysis of the properties of the fiber tow

As illustrated in Figure 5, the major purpose of micro-scale analysis was to obtain the elastic constants and strength values of the fiber yarn, which would later be assigned to the fiber tow during the meso-scale analysis. The multi-scale analyses began with the construction of the corresponding representative volume elements (RVE) for micro- and meso-scale analysis. The

meso-scale and micro-scale RVEs (Figure 7) were built using *Solidworks*. Details on the construction of the RVEs using *Solidworks* can be found in Ref. [14, 21]. Carbon fiber was the major load-bearing constituent. The major concern when building the meso-scale and micro-scale RVEs is to make sure that the correct fiber volume fraction is achieved. The global fiber volume fraction, V_{global}, of the composite face-sheet of the landing gear can be expressed as follows:

$$V_{global} = V_{tow} \times V_f \tag{1}$$

Where, V_{tow} is volume fraction of the fiber tow in the meso-scale representative volume element and V_f is the volume fraction of the carbon fiber in single fiber yarn. The global fiber volume fraction of the landing gear was 63.6%. The fiber volume fraction in the fiber yarn was arbitrarily decided as 85% (this fiber volume fraction does not affect the computation accuracy and can be achieved by current fabrication technique). The volume fraction of the fiber tow inside the meso-scale RVE was 74.8%.

In Figure 7, the geometry of the fiber yarn of the fiber tow was measured for the real braided architecture. Once the fiber tow was established, the matrix block was built such that the target fiber volume fraction was achieved. A micro-scale RVE was extracted from hexagonal array of fibers. As depicted in Figure 7e, r is the diameter of the carbon fiber while a_1 and a_2 are the width and length of the RVE, respectively, where $2\pi r^2$/ (a1∗a2) =85% such that the target fiber volume fraction was achieved.

The elastic properties as well as the strength values of A-42 carbon fiber, L20 epoxy resin and their interface were obtained experimentally in our previous studies [21]. These values which are used as inputs for the finite element analysis are summarized in Tables 2-4.

Four-node tetrahedron elements (C3D4) were adopted for the meshing of both the fiber and matrix of the micro-scale RVE. For the calculation of the elastic constants and the strength

values of the fiber yarn, the periodic boundary conditions devised by Ji et al. [22] were adopted. In the micro-scale model, maximum stress failure criterion was considered to be appropriate in describing the damage initiation in carbon fibres. It can be expressed as:

$$\sigma_f \le X_{fT}\,(\sigma_f \ge 0)\, or - \sigma_f \le X_{fC}\,(\sigma_f < 0) \tag{2}$$

Where, X_{fT} and X_{fC} are the tensile and compressive strength, respectively, subscript 'f' represents the quantity of the fiber. σ_f is the normal stress component along the longitudinal direction of the fiber. When failure to the fiber was identified, the properties of the carbon fiber would be reduced to 0.1% (near zero due to the brittle nature of carbon fiber).

A modified von Mises criterion (the Stassi's criterion) was employed to define the failure in the matric block for both the micro- and meso-scale models. The Stassi's criterion for materials with different strengths in compression and tension is expressed as:

$$\left[\frac{1}{X_{mT}} - \frac{1}{X_{mC}}\right](\sigma_1 + \sigma_2 + \sigma_3) + \frac{1}{X_{mT}} \times \frac{1}{X_{mC}} \left\{\frac{1}{2}\left[(\sigma_1 - \sigma_2)^2 + (\sigma_2 - \sigma_3)^2 + (\sigma_3 - \sigma_1)^2\right]\right\} \le 1 \tag{3}$$

or,

$$\left[\frac{1}{X_{mT}} - \frac{1}{X_{mC}}\right] 3P + \frac{1}{X_{mT}} \times \frac{1}{X_{mC}} \sigma_{vm}^2 \le 1 \tag{4}$$

Where, σ_1, σ_2 and σ_3 are principal stresses along three directions. The term 'P' refers to the hydrostatic pressure and σ_{vm} refers to the Von Mises stress components. X_{mT} and X_{mC} are the tensile and compressive strength of the matrix resin. When failure in matrix resin was detected, the Young's modulus of the resin would be reduced to 40%.

3.2 Meso-scale analysis of the properties of bi-axial braids

There were three braiding angles as seen in Figure 4b. The purpose of meso-scale analysis was to obtain the elastic constants and strength values of the composite face-sheet of the landing gear, which included bi-axial braids of 33°, 35° and 37.2°. The geometries of the bi-axial meso-

scale RVEs were created using *Solidworks*. The fiber yarn in the meso-scale RVE was modelled as transversely isotropic material. The elastic constants of the fiber yarn, which were calculated via micro-scale analysis, together with the properties of epoxy resin were used as inputs for meso-scale analysis. Both the fiber tow and matrix resin in the meso-scale RVE were meshed with four-node tetrahedron elements (C3D4).

More detailed information on meso-scale analysis was discussed in Ref. [14, 21]. Progressive damage analysis was performed during meso-scale analysis. The damage initiation and subsequent material property degradation was implemented by using USDFLD user subroutine. The degradation scheme for meso-scale analysis is summarized in Figure 6. Hashin's failure criteria in 3D form, which are failure criteria based on failure modes [17], were used for the analysis of the fiber yarn in the fiber tow:

Fiber failure in tension ($\sigma_{11} > 0$): $\left(\frac{\sigma_{11}}{X_{yT}}\right)^2 + \frac{\tau_{12}^2 + \tau_{13}^2}{\left(S_{y12}\right)^2} \le 1$ (5)

Fiber failure in compression ($\sigma_{11} < 0$): $\left|\sigma_{11}\right| \le X_{yC}$ (6)

Matrix failure in tension ($\sigma_{22} + \sigma_{33} > 0$):

$$\left(\frac{\sigma_{22} + \sigma_{33}}{Y_{yT}}\right)^2 + \frac{\tau_{23}^2 - \sigma_{22}\sigma_{33}}{\left(S_{y23}\right)^2} + \frac{\tau_{12}^2 + \tau_{13}^2}{\left(S_{y12}\right)^2} \le 1 \quad (7)$$

Matrix failure in compression ($\sigma_{22} + \sigma_{33} < 0$):

$$\left[\left(\frac{Y_{yC}}{2S_{y23}}\right)^2 - 1\right]\frac{\sigma_{22} + \sigma_{33}}{Y_{yC}} + \left(\frac{\sigma_{22} + \sigma_{33}}{2S_{y23}}\right)^2 + \frac{\tau_{23}^2 - \sigma_{22}\sigma_{33}}{\left(S_{y23}\right)^2} + \frac{\tau_{12}^2 + \tau_{13}^2}{\left(S_{y12}\right)^2} \le 1 \quad (8)$$

Where, the subscript '*y*' represent the quantity of the fiber yarn.

3.3 Macro-scale analysis of the flexural properties of the landing gear

The geometry of the composite face-sheets as well as the foam core were built using a commercial CAD software, *Solidworks* (Figure 8). The foam core was treated as isotropic

material. The Young's modulus and Poisson's ratio of the PU 4507 foam core was 67.3 MPa and 0.09, determined experimentally and estimated, respectively. The composite face sheet was treated as orthotropic material. As seen in Figure 4, there were 5 sections on the composite face-sheet depending on the braiding angle of individual section. The elastic constants and strength values of bi-axial braids of different braiding angles were computed through meso-scale analyses and assigned to individual sections of the composite face-sheets.

As seen in Figure 3, the two legs of the landing gear could move freely along the 'x' axis. Corresponding boundary conditions were applied during FEA analysis as shown in Figure 9. The two ends were allowed to move freely along 'x' direction. Movements of the two ends along the other two directions were prohibited. The flexure load was applied to the landing gear as displacement. As shown in Figure 9, 100mm of displacement was applied to the center of the landing gear.

For the prediction of the peak flexure load of the landing gear, progressive damage analyses were carried out. During each iteration or increment in displacement, the stress field of the landing gear was computed by the ABAQUS solver. Possible failure inside the structure was identified by maximum stress failure criteria as expressed in Equation (9), where the subscript '*b*' represents the relevant parameters of the braids of the face-sheet. As seen in Equation (9), if the absolute value of any stress component (e.g., σ_{11}) exceeds the relevant strength value, the material would fail and the failure index would be either equal to or greater than 1. The maximum stress failure criteria were coded in USDFLD user subroutine using Fortran 77 programming language. When failure was detected (failure index ≥ 1) due to certain failure modes (e.g., failure due to compression), the elastic constants of the material would be degraded through the usage of solution-dependent state variables and field variables. The general material

property degradation strategy was that if the failure was detected the elastic constants would be reduced to 1% of their original magnitude. The stiffness matrix of the material would be updated and return to the ABAQUS solver for the stress analysis of the next iteration.

$$Failure\,index = \max\left\{\begin{array}{c} \frac{\sigma_{11}}{X_{bT}} if\ \sigma_{11} > 0 or -\frac{\sigma_{11}}{X_{bC}} if\ \sigma_{11} < 0 \\ \frac{\sigma_{22}}{Y_{bT}} if\ \sigma_{22} > 0 or -\frac{\sigma_{22}}{Y_{bC}} if\ \sigma_{22} < 0 \\ \frac{\sigma_{33}}{Z_{bT}} if\ \sigma_{33} > 0 or -\frac{\sigma_{33}}{Z_{bC}} if\ \sigma_{33} < 0 \\ abs\left(\frac{\tau_{12}}{S_{b12}}\right) \\ abs\left(\frac{\tau_{23}}{S_{b23}}\right) \\ abs\left(\frac{\tau_{31}}{S_{b31}}\right) \end{array}\right\} \quad (9)$$

4. Results and discussions

4.1 Micro-scale analysis

The elastic constants of the fiber yarn predicted by micro-scale analysis are summarized in Table 5. It should be noted that subscript '*y*' represents quantity of the fiber yarn while subscript '*f*' represents the quantity of the fiber. Analytically, these properties can be determined through the Chamis equation [23] as:

$$E_{y11} = V_f E_{f11} + (1 - V_f) E_m \quad (10)$$

$$E_{y22} = E_{y33} = -\frac{E_m}{1 - \sqrt{V_f}\left(1 - \frac{E_m}{E_{f22}}\right)} \quad (11)$$

$$G_{y12} = G_{y13} = -\frac{G_m}{1 - \sqrt{V_f}\left(1 - \frac{G_m}{G_{f12}}\right)} \quad (12)$$

$$G_{y23} = -\frac{G_m}{1 - \sqrt{V_f}\left(1 - \frac{G_m}{G_{f23}}\right)} \quad (13)$$

$$\upsilon_{y12} = \upsilon_{y13} = V_f \upsilon_{f12} + (1 - V_f)\upsilon_m \tag{14}$$

$$\upsilon_{y23} = \frac{E_{f22}}{2G_{f23}} - 1 \tag{15}$$

As seen in Table 5, the elastic constants predicted by the micro-scale FEA model were reasonably close to that calculated by Chamis equation. The strength values of the fiber yarn were predicted through the micro-scale FEA model and summarized in Table 6. These strength values would be used during programming of the USDFLD user subroutine during meso-scale analysis.

4.2 Meso-scale analysis

The elastic constants and strength values of bi-axial braids of various braiding angles calculated through meso-scale analysis are summarized in Tables 7 and 8. It should be noted that subscript '*b*' represents the quantity of bi-axial braids. The elastic constants were assigned to the composite face-sheet of the landing gear during the macro-scale analysis while the strength values presented in Table 8 were used in USDFLD subroutines to define failures to the landing gear.

The major concern during progressive damage analysis was the selection of appropriate failure criteria and subsequent material property degradation scheme. A case study was implemented to verify the accuracy of the meso-scale model. Tensile coupons of the same material of the composite face-sheet of the landing gear were fabricated and tested using MTS 810 Material Test System. The braiding angle of these coupons was 30°. Meso-scale RVE of 30° was built and progressive damage analysis was carried out.

The tensile stress/strain curve predicted by FEA analysis was compared in Figure 10 with experimentally observed response. As seen in Figure 10, the predicted tensile strength is very close to the tensile strength obtained through tensile tests. The predicted tensile strength is

498.35 MPa. The average tensile strength measured by tensile tests is 485.85±20.77 MPa. The current meso-scale FEA model successfully predicted the tensile strength of bi-axial braided composites.

As seen in Figure 10, the simulated curve initially coincides closely with the two experimental curves. After point ‘a’ (~0.7% of strain) in Figure 10, change in the slope of the simulated curve is observed. The failure status of the meso-scale RVE corresponding to 0.7% of strain is shown in Figure 11. As seen in Figure 11a, when the strain was 0.7% the carbon fiber did not fail. However, failure of the resin in both the fiber tow and the pure matrix block is predicted. The FEA model is very sensitive to the failure of individual constituents. Once failure was detected, the degradation of the corresponding elastic constants would be carried out. This explains why the slope of the simulated curve decreases after point ‘a’ in Figure 10.

As illustrated in Figure 11, the meso-scale model predicted that failure of the epoxy resin occurred earlier than that of the carbon fiber. This phenomenon matched well with experimental results. During the course of tensile tests, the first damage was usually observed in the matrix resin rather than in the carbon fiber. As shown in Figure 12b, necking in the sample was gradually observed under tensile loading while the fiber was still intact. The necking in the sample became more and more severe as the testing continued until eventually breakage of fiber tow occurred which led to the complete breakage of the coupon. The extensometer slipped when necking was observed. This explains why the post-peak match between simulation and experiment was not as good as the initial comparison. With proper failure criteria and material degradation scheme, the meso-scale FEA model could successfully predict the strength and failure modes of bi-axial braided composites.

4.3 Macro-scale analysis

The predicted curve for the landing gear under bending load is plotted in Figure 13 in

comparison with the experimental curve. The magnitude of the slope of the initial linear portion of the flexure load vs. flexure extension curve depends on the overall stiffness (the various elastic constants) of the landing gear. As seen in Figure 13, the initial linear portions of the experimental and FEA curves coincide well with each other, indicating that correct elastic constants were provided to the ABAQUS software. The meso-scale analyses successfully predicted the elastic constants of the braids with different braiding angles, which was crucial for the subsequent macro-scale analysis.

In the meantime, the peak flexure load has been successfully predicted by the multi-scale FEA analysis as seen in Figure 13. The average peak flexure load measured by experiments was 891.6N, while the peak flexure load predicted by progressive damage analysis was 888.1N. This apparently proves the effectiveness of the current FEA model. It is noted that the flexure extension corresponding to peak flexure load predicted by FEA analysis was smaller than experimental observation. The indentation of the loading bar could be one of the possible reasons.

For progressive damage analysis, there are two factors that should be properly addressed for the successful prediction of the peak flexure load. First, appropriate failure criteria that reflect the actual major failure modes of the composite structure should be used. Second, correct strength values (e.g., tensile strength, compressive strength) should be provided to the USDFLD subroutine which is used to identify and define various failure mechanisms. In this investigation, maximum stress criteria were selected as the failure criteria while the various strength values of the bi-axial braids of the composite face-sheet of the landing gear were obtained through meso-scale analysis.

One of the purposes of progressive damage analysis is to predict the failure modes after peak

load point. This purpose is successfully fulfilled in the current work. Sudden drops in flexure load are seen in Figure 13 on the experimental curve which indicates that the landing gear exhibited brittle behavior under bending load. After the peak flexure load point, the pattern of the FEA curve is fairly similar to that of the experimental curve. The failure modes of the landing gear structure under bending load are discussed in details in Figures 14-17.

In the current FEA model, field variables (*fv*) are used to represent failures in the landing gear. When a failure criterion is fulfilled the corresponding field variable will be equal to 1 ($fv(i)=1$). When damages occur, the stiffness would decrease and the flexure load decreases with flexure extension on the respective flexure load vs. flexure extension curve. The failure contour of the landing gear was observed during FEA analysis. FEA analysis revealed that the major failure modes were compression failure at the top surface (the surface which was in contact with the loading bar) and tensile failure at the bottom surface. Moreover, it is also found that failure on the top surface (due to compression) occurred earlier than failure on the bottom surface (due to tension). In Figure 14, failure contours corresponding to point 'A' (at which the flexure extension was 60mm and measured time was approximately 3600 seconds) and point 'B' (at which the flexure extension was 80mm and measured time was approximately 4800 seconds) are included. As seen in Figure 14, failure on the top surface increased while no failure was observed on the bottom surface even until the flexure extension was 80mm. The failure contour predicted by the FEA model is supported by experimental observation. Both the top and bottom surface were closely observed during the course of bending test. Photos of both the top and bottom surfaces during experiment after the peak flexure load point are presented in Figure 15. It is clearly see in Figure 15 that damages to the top surface already occurred due to compression (Figure 15a) while no damage was identified on the bottom surface (Figure 15b).

As seen in Figure 16, damages on the bottom surface appeared as the flexure extension increased (the loading bar further moved down). Damages on the bottom surface began to take place due to tension at a much larger flexure extension as compared with damages on the top surface. In the meantime, the top surface experienced more severe damage than the bottom surface as seen in Figure 16 (point ‘C’ in Figure 16 which approximately corresponds to 6000 seconds of measured time). This finding is also supported by experimental observations. Photos of both the top and bottom surface of the landing gear after bending test are presented in Figure 17. Breakage of fiber tow was observed on the bottom surface. Damages on the top surface were apparently more evident as compared with that on the bottom surface. Moreover, as seen in Figure 17, the damage contours predicted by the FEA model matched well with experimental observations.

5. Conclusions

Braided textile composite landing gear structures, which were designed for unmanned aerial vehicle, were successfully fabricated and tested under bending loads. A multi-scale FEA model aimed at progressive damage analysis was developed for the prediction of the flexural behavior of the landing gear structure that was made of A42 carbon fiber/L20 epoxy composites. The developed model aimed at linking the properties of the constituents measured experimentally in this work to that of the entire structure. Progressive damage analysis was carried out at micro-scale and meso-scale levels to calculate the properties of fiber tows and bi-axially braided composites, respectively. During each level of analysis, appropriate failure criteria were selected and coded into the USDFLD user subroutine, which, together with a material property degradation scheme, identified failure in the elements and reduced the material property accordingly. The results of the micro-scale and meso-scale analyses eventually served as inputs

for macro-scale analysis which predicted the mechanical properties of the whole structure.

The flexure load vs. extension curve, peak flexure load and damage contours predicted by the FEA analysis were compared with the experimental results. Good agreement between the FEA analyses and experimental observations was achieved, proving the accuracy of the multi-scale FEA model developed in this work. More importantly, the modelling methodology used in the current study can also be used in the analysis of other composite structures under different loading conditions.

Conflict of Interest

The authors declare that they have no conflict of interest.

Acknowledgement

This research was carried out at the Temasek Laboratories @ NTU, Nanyang Technological University, Singapore. The authors would like to thank Temasek Laboratories @ NTU for the support during this research.

References

[1] Pastore CM. Opportunities and challenges for textile reinforced composites. *Mechanics of Composite Materials* 2000; 36(2): 97-116.

doi: 10.1007/BF02681827

[2] Zhou LD, Zhuang Z. Strength analysis of three-dimensional braided T-shaped composite structures. *Composite Structures* 2013; 104: 162-168.

doi: 10.1016/j.compstruct.2013.04.023

[3] Zhou H, Pan Z, Gideon RK, Gu B, Sun B. Experimental and numerical investigation of the transverse impact damage and deformation of 3-D circular braided composite tubes from meso-structure approach. *Composites Part B: Engineering* 2016; 86: 243-253.

doi: 10.1016/j.compositesb.2015.10.019

[4] Ren J, Kim YK, Rice J. Comparing the fracture toughness of 3-D braided preform composites with z-fiber-reinforced laminar composites. *Textile Research Journal* 2011; 81(4): 335-343.

doi: 10.1177/0040517510385172

[5] Kim KJ, Yu W-R, Lee JS, Gao L, Thostenson ET, Chou T-W, Byun J-H. Damage characterization of 3D braided composites using carbon nanotube-based in situ sensing. *Composites Part A: Applied Science and Manufacturing* 2010; 41(10): 1531-1537.

doi: 10.1016/j.compositesa.2010.06.016

[6] Poe CC, Dexter HB, Raju IS. Review of the NASA textile composites research. *Journal of Aircraft* 1999; 36(5): 876-884.

doi: 10.2514/2.2521

[7] Sevenois RDB, Van Paepegem W. Fatigue damage modelling techniques for textile composites: Review and comparison with unidirectional composite modelling techniques. *Applied Mechanics Reviews* 2015; 67(2), article number 020802.

doi: 10.1115/1.4029691

[8] Fang G, Liang J. A review of numerical modeling of three-dimensional braided textile composites. *Journal of Composite Materials* 2011; 45(23): 2415-2436.

doi: 10.1177/0021998311401093

[9] Xu K, Qian X. A new analytical model on predicting the elastic properties of 3D full five-directional braided composites based on a multiunit cell model. *Composites Part B: Engineering* 2015; 83: 242-252.

doi:10.1016/j.compositesb.2015.08.052

[10] Han H, Taheri F, Pegg N, Lu Y. A numerical study on the axial crushing response of hybrid pultruded and ±45° braided tubes. *Composite Structures* 2007; 80(2): 253-264.
doi: 10.1016/j.compstruct.2006.05.012

[11] Sun J, Wang Y, Zhou G, Wang X. Finite Element Analysis of Mechanical Properties of 3D Surface-Core Braided Composites. *Polymer Composites* 2016; Article in press.
doi: 10.1002/pc.24035

[12] Liu P, Liu XJ, Zhou Y, Huo B, Zhang SX. Effect of fibre braiding orientation on the natural frequency of 2D braided composites cantilever beam. *Materials Research Innovations* 2015; 19: 33-37.
doi: 10.1179/1432891715Z.0000000002081

[13] Zhang M, Zuo C, Sun B, Gu B. Thermal ageing degradation mechanisms on compressive behavior of 3-D braided composites in experimental and numerical study. *Composite Structures* 2016; 140: 180-191.
doi:10.1016/j.compstruct.2016.01.029

[14] Nobeen NS, Zhong Y, Francis BAP, Ji X, Chia ESM, Joshi SC, Chen Z. Constituent materials micro-damage modeling in predicting progressive failure of braided fiber composites. *Composite Structures* 2016; 145: 194-202.
doi: 10.1016/j.compstruct.2016.02.078

[15] Wan Y, Wang Y, Gu B. Finite element prediction of the impact compressive properties of three-dimensional braided composites using multi-scale model. *Composite Structures* 2015; 128: 381-394.
doi:10.1016/j.compstruct.2015.03.066

[16] Xiao X, McGregor C, Vaziri R, Poursartip A. Progress in braided composite tube crush

simulation. *International Journal of Impact Engineering* 2009; 36(5): 711-719.
doi: 10.1016/j.ijimpeng.2008.09.006

[17] Hashin Z. Failure criteria for unidirectional fiber composites. *Journal of Applied Mechanics* 1980; 47(2): 329-334.
doi: 10.1115/1.3153664

[18] Madukauwa-David ID, Drissi-Habti M. Numerical simulation of the mechanical behavior of a large smart composite platform under static loads. *Composites Part B: Engineering* 2016; 88: 19-25.
doi: 10.1016/j.compositesb.2015.10.041

[19] Dai S, Cunningham PR. Multi-scale damage modelling of 3D woven composites under uni-axial tension. *Composite Structures* 2016; 142: 298-312.
doi:10.1016/j.compstruct.2016.01.103

[20] Panamoottil SM, Das R, Jayaraman K. Anisotropic continuum damage model for prediction of failure in flax/polypropylene fabric composites. *Polymer Composites* 2015, Article in Press.
doi: 10.1002/pc.23453

[21] Wang C, Zhong Y, Bernad Adaikalaraj PF, Ji X, Roy A, Silberschmidt VV, Chen Z. Strength prediction for bi-axial braided composites by a multi-scale modelling approach. *Journal of Materials Science* 2016; 51(12): 6002-6018.
doi: 10.1007/s10853-016-9901-z

[22] Ji X, Khatri AM, Chia ES, Cha RK, Yeo BT, Joshi SC, Chen Z. Multi-scale simulation and finite-element-assisted computation of elastic properties of braided textile reinforced composites. *Journal of Composite Materials* 2014; 48(8): 931-949.
doi: 10.1177/0021998313480198

[23] Chamis C. Mechanics of Composite Materials: Past, Present, and Future. *Journal of Composites, Technology and Research* 1989; 11(1), pp. 3-14.

doi: 10.1520/CTR10143J

Figures

Figure 11 Failure status of the meso-scale RVE at the strain of 0.7% showing that failure of the resin in both the fiber tow and the pure matrix block occurred while no fiber damage was observed.

Figure 12 Failure characteristics of bi-axial braided composite coupons with a braiding angle of 30^{o} under tensile load: (a) beginning of tensile test; (b) necking occurred; (c) final breakage.

Figure 13 Flexural behavior of the landing gear-comparison between the experimental curve and the curve obtained through multi-scale FEA analysis.

Figure 14 Predicted damage distribution on the landing gear showing that failure on the top surface due to compression occurred while no damage was observed on the bottom surface.

Figure 15 Photographs of the landing gear during bending test after the peak flexure load was reached: a) top surface; b) bottom surface.

Figure 16 Predicted damage distribution on the landing gear showing that failure on the bottom surface due to tension occurred at the end of the bending event.

Figure 17 Damages to the landing gear under bending load-comparison between predicted damage contours and experimental observations.

Tables

Table 1 Summary of the bending test result of the landing gear structures

Table 2 Properties of A-42 carbon fibers as inputs for micro-scale model

Table 3 Properties of epoxy resin

Table 4 Properties of carbon fiber/epoxy interface as inputs for micro-scale model

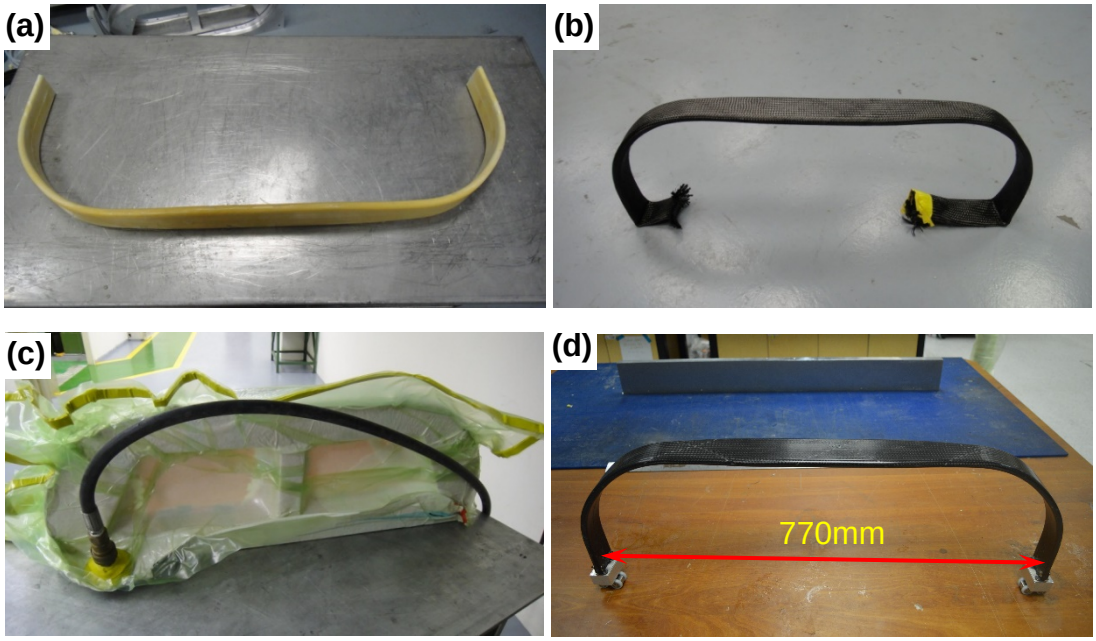

Figure 1 Fabrication of the landing gear structure: (a) foam core; (b) foam core wrapped by A-42 carbon fiber sleeves; (c) vacuum bag assembly which includes the landing gear and the aluminum mold; (d) fabricated landing gear structure.

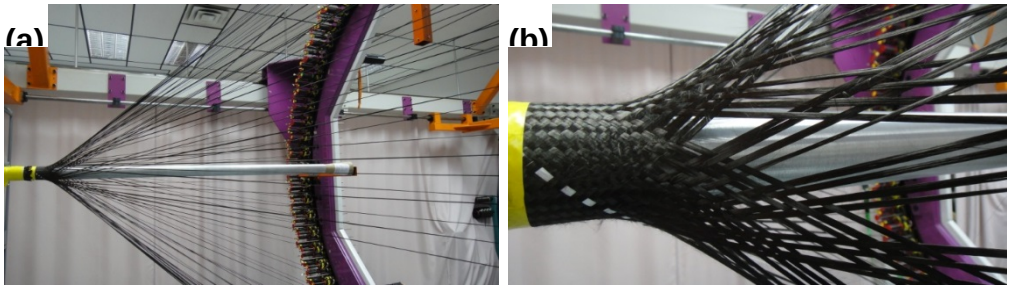

Figure 2 Processing of the carbon fiber sleeve using a braiding machine.

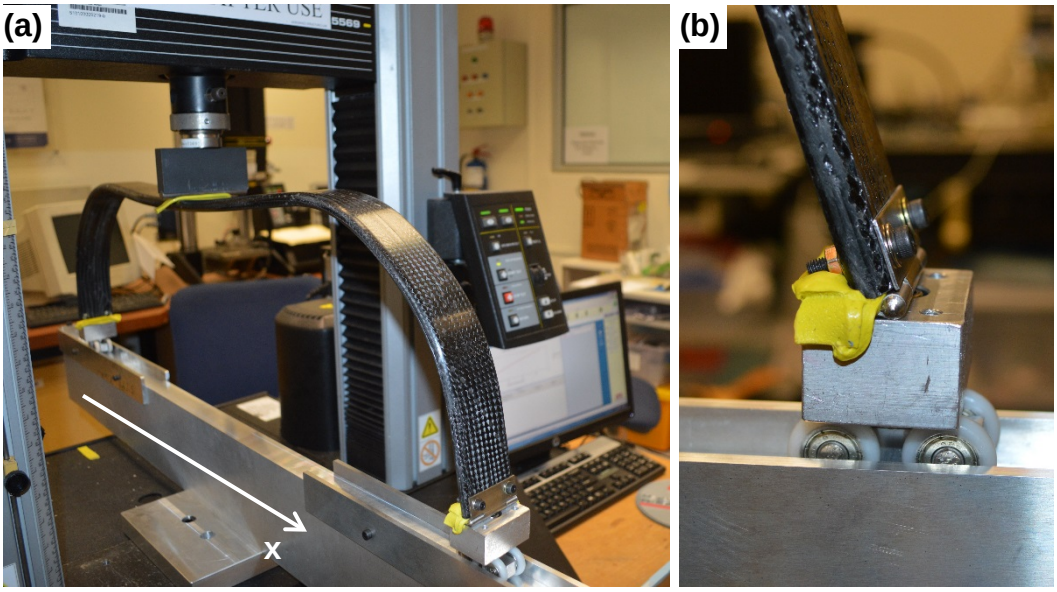

Figure 3 A landing gear under bending test: a) overall testing set-up; b) Teflon wheels used to support the landing gear.

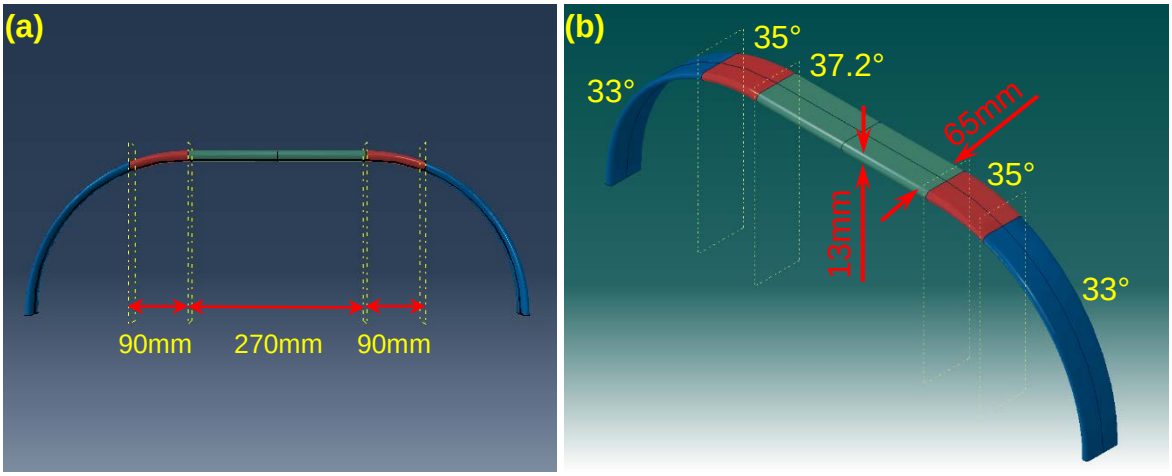

Figure 4 Braiding angles of different sections of the composite face-sheet of the landing gear

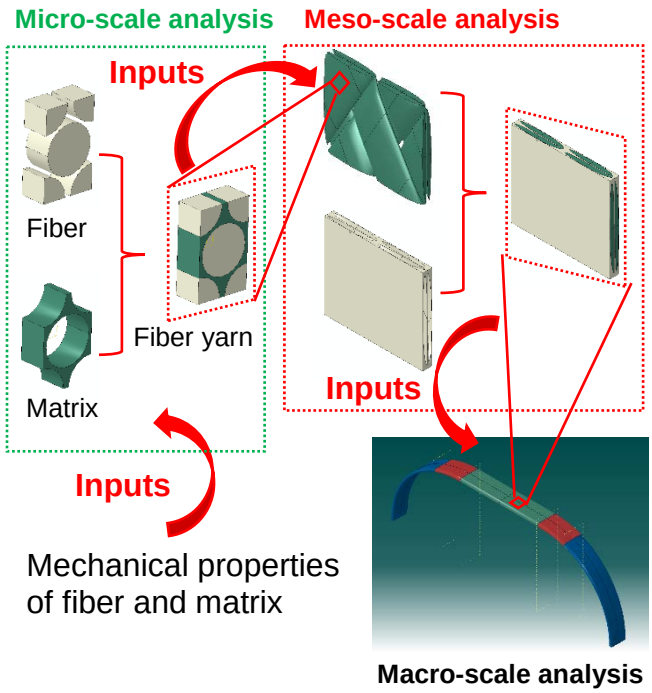

Figure 5 Flowchart of the multi-scale model for the prediction of the bending behavior of the landing gear structure

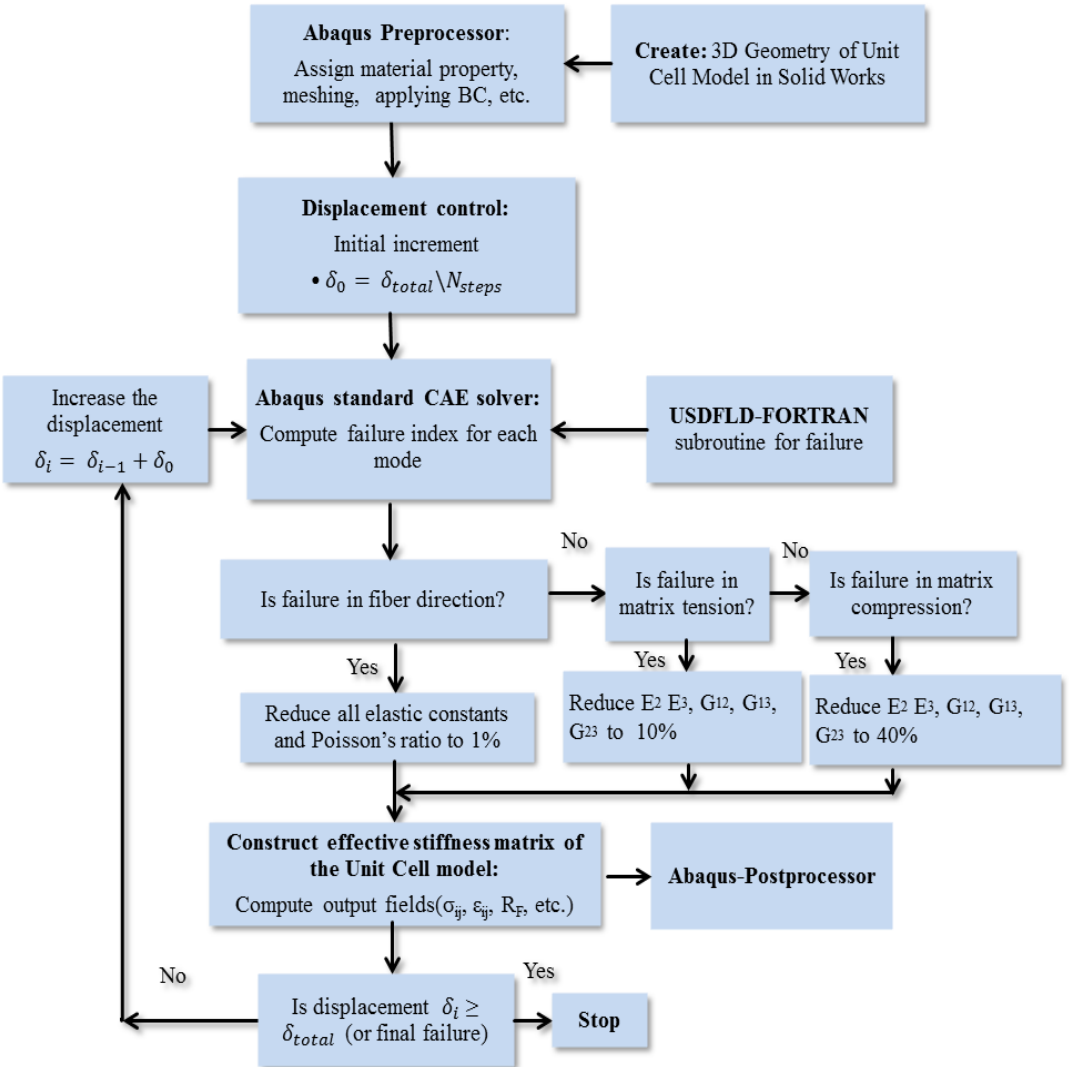

Figure 6 Flow chart of progressive damage analysis for meso-scale modelling which computes homogenized properties for the composite face-sheet of the landing gear structure

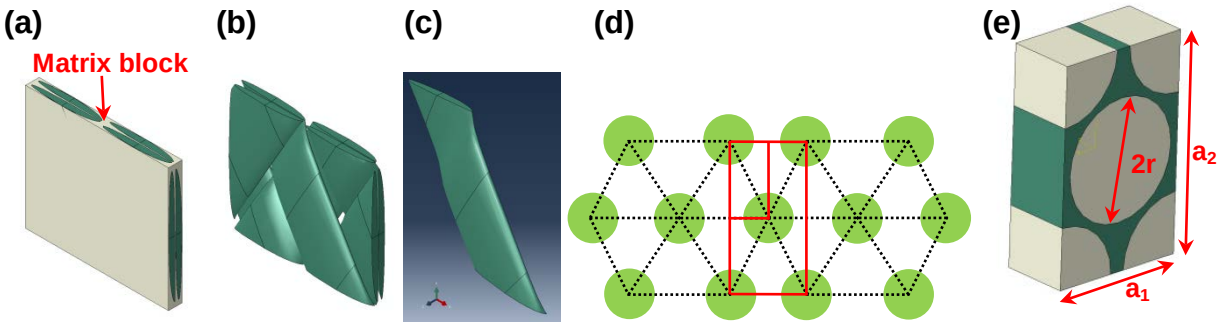

Figure 7 Construction of representative volume elements (RVE): (a) meso-scale RVE; (b) fiber tow of a meso-scale RVE; (c) single fiber yarn; (d) Hexagonal array of fibers in a fiber yarn; (e) micro-scale RVE extracted from hexagonal array of fibers.

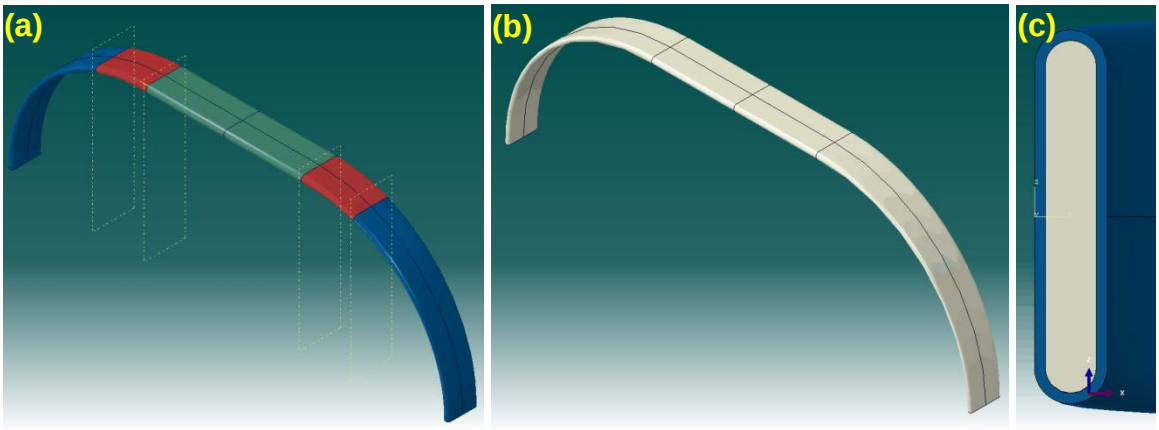

Figure 8 Composite face sheet and foam core of the landing gear created by *Solidworks*: (a) composite face sheet; (b) foam core; (c) cross-section of the landing gear.

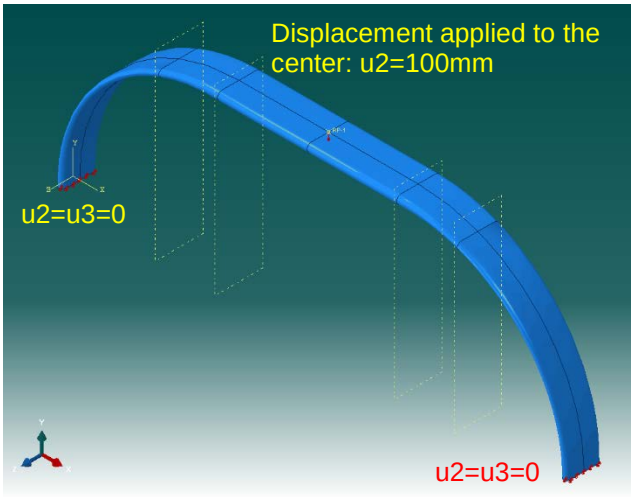

Figure 9 Boundary conditionings applied during the macro-scale analyses on the bending behavior of the landing gear

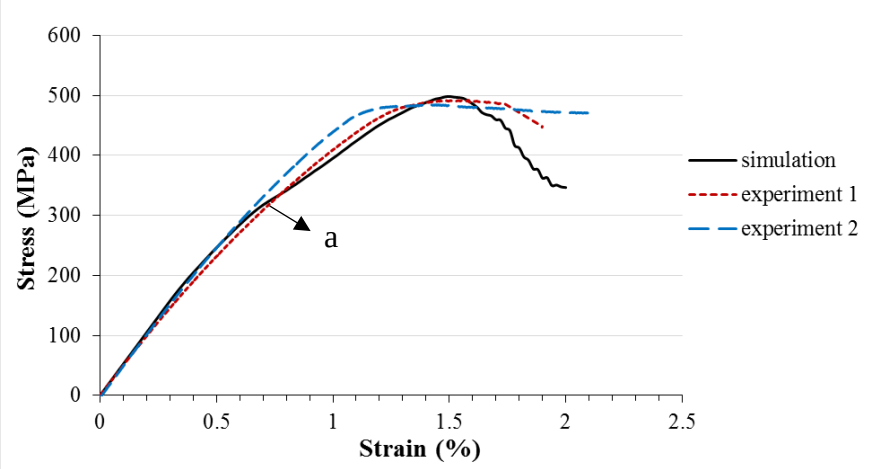

Figure 10 Tensile stress vs. strain curve of bi-axial braided composites with a braiding angle of 30º: comparison between experiments and FEA analysis.

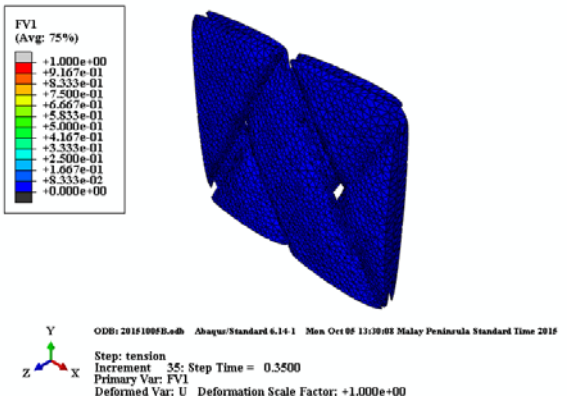

(a) Failure status of the fibers in the fiber tow

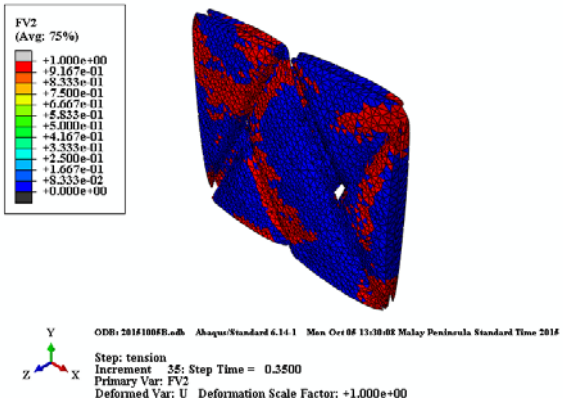

(b) Failure status of the resin in the fiber tow

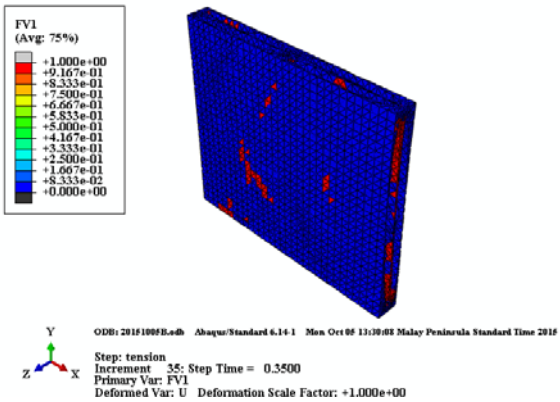

(c) Failure status of the pure matrix block

Figure 11 Failure status of the meso-scale RVE at the strain of 0.7% showing that failure of the resin in both the fiber tow and the pure matrix block occurred while no fiber damage was observed.

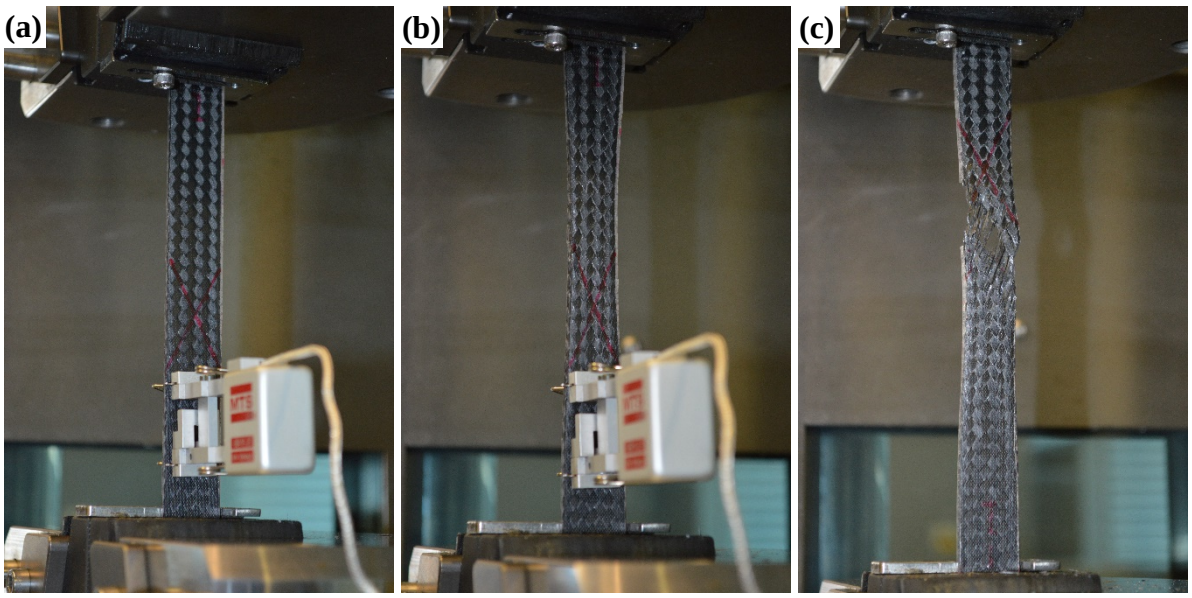

Figure 12 Failure characteristics of bi-axial braided composite coupons with a braiding angle of 30º under tensile load: (a) beginning of tensile test; (b) necking occurred; (c) final breakage.

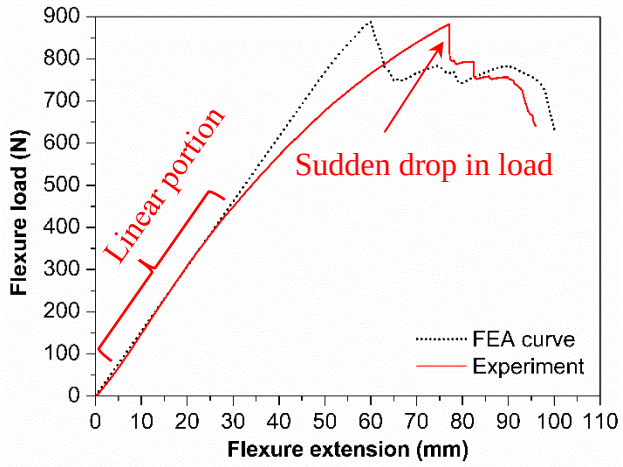

Figure 13 Flexural behavior of the landing gear-comparison between the experimental curve and the curve obtained through multi-scale FEA analysis.

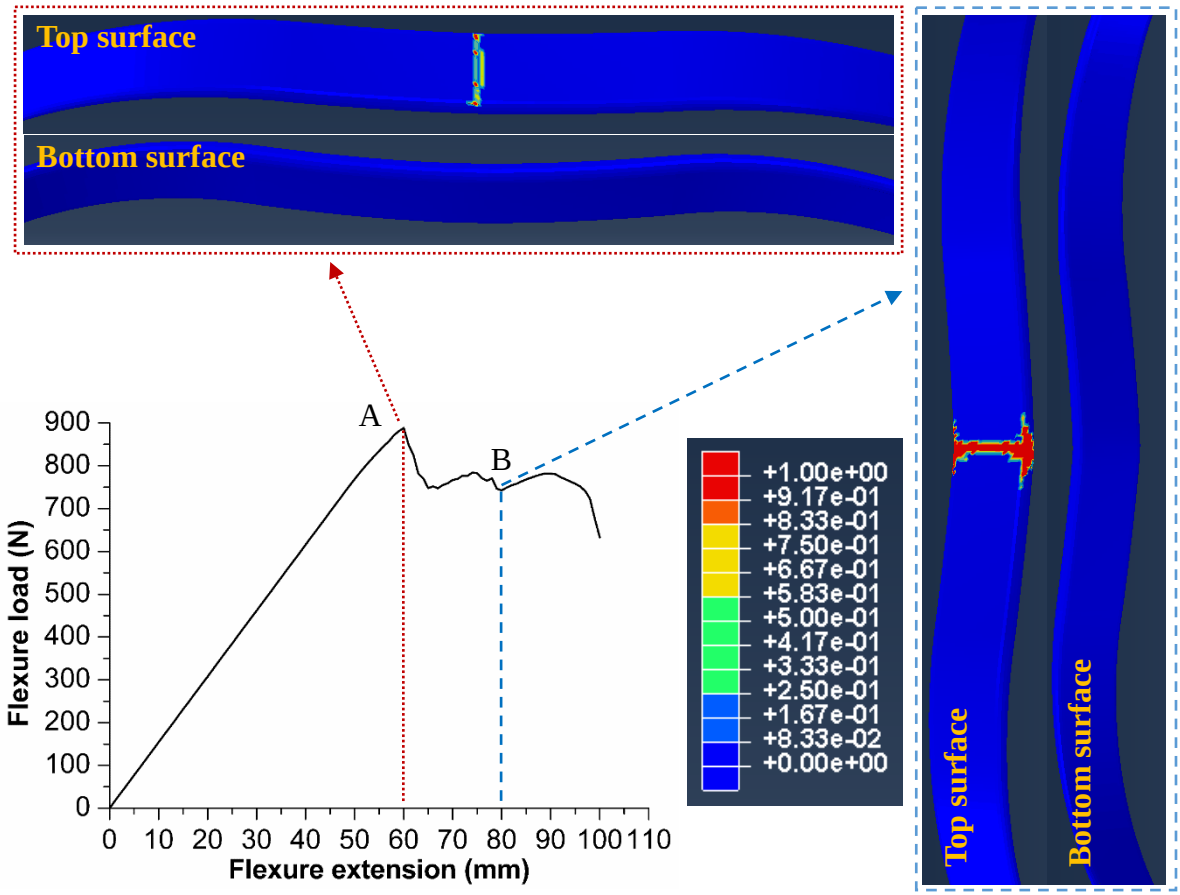

Figure 14 Predicted damage distribution on the landing gear showing that failure on the top surface due to compression occurred while no damage was observed on the bottom surface.

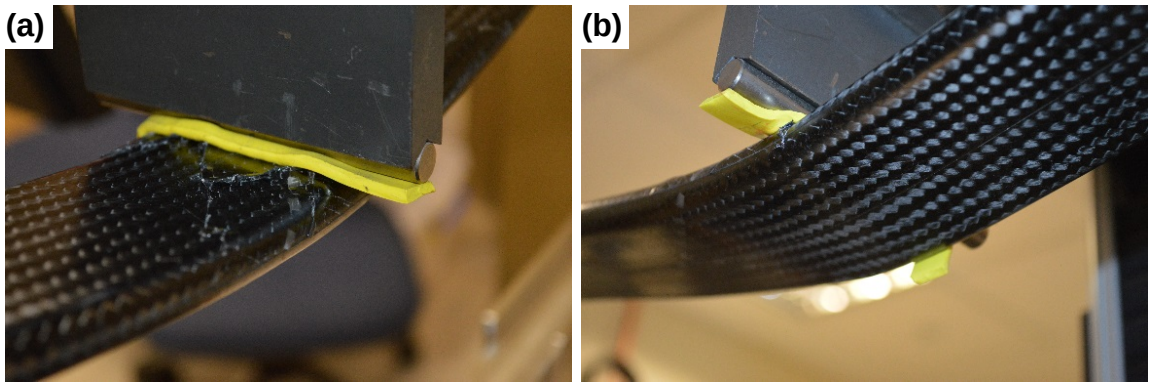

Figure 15 Photographs of the landing gear during bending test after the peak flexure load was reached: a) top surface; b) bottom surface.

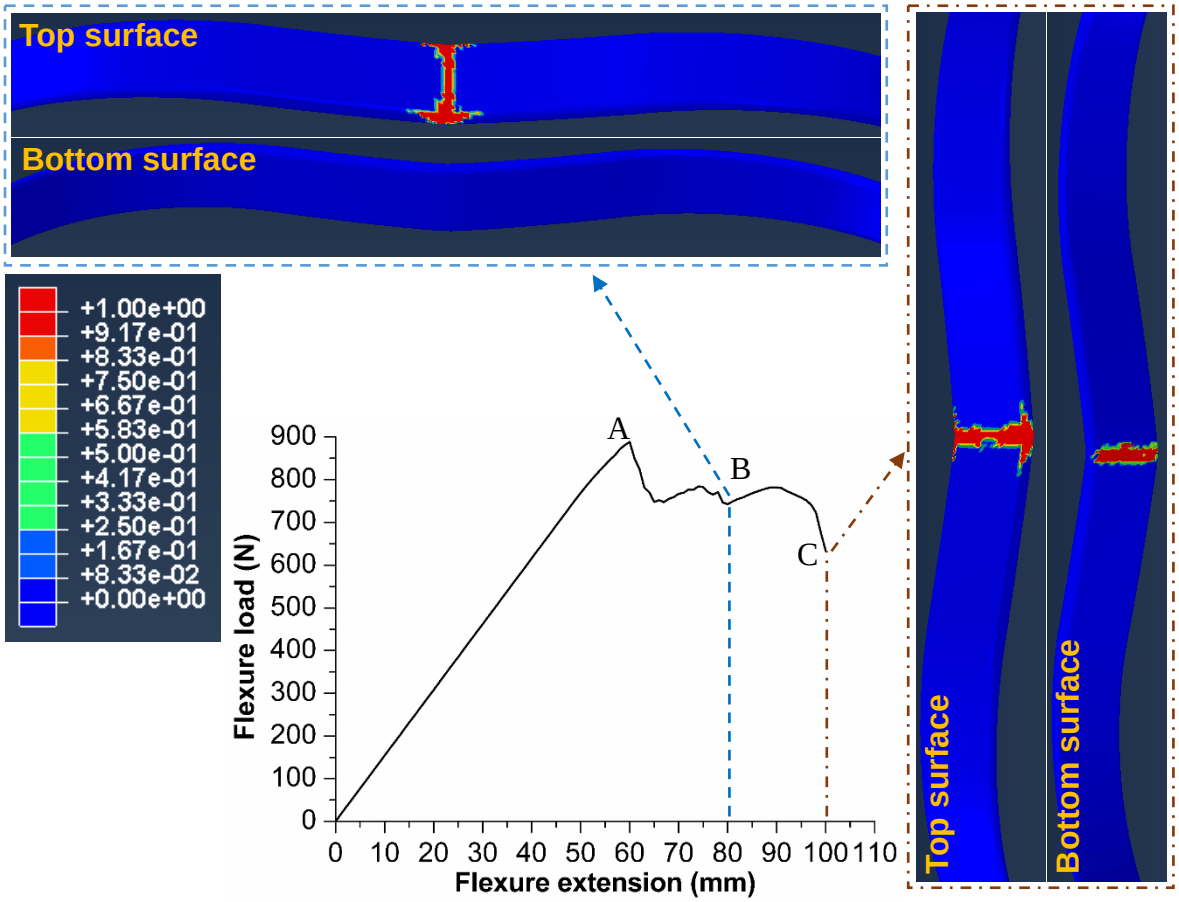

Figure 16 Predicted damage distribution on the landing gear showing that failure on the bottom surface due to tension occurred at the end of the bending event

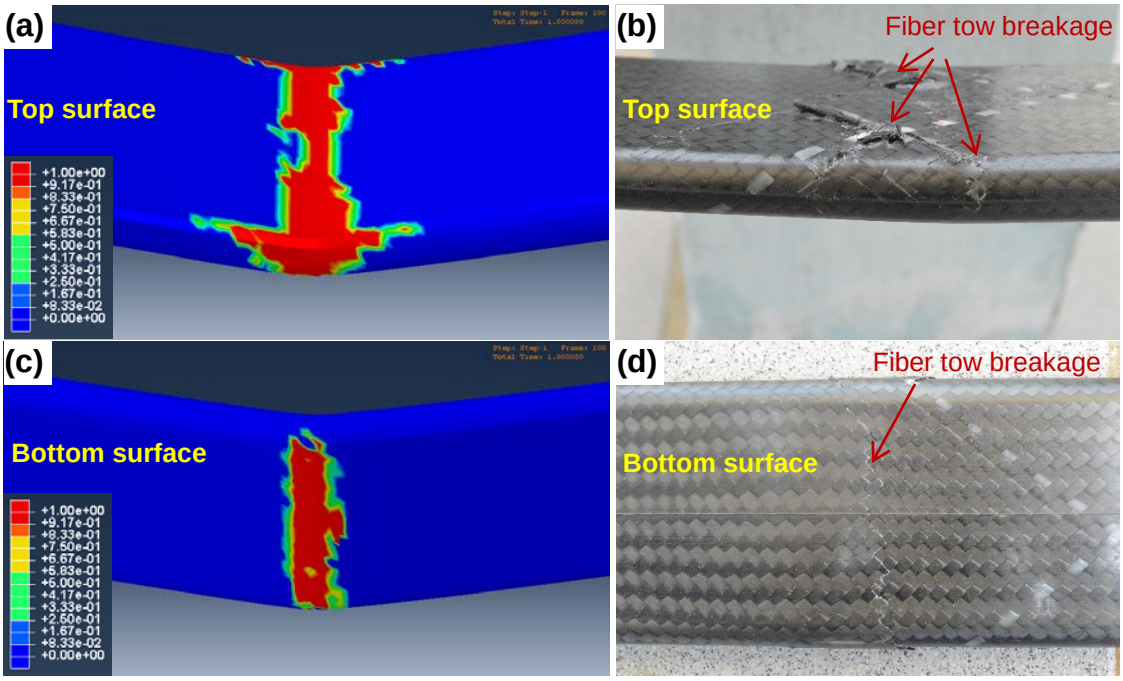

Figure 17 Damages to the landing gear under bending load-comparison between predicted damage contours and experimental observations

Table 1 Summary of the bending test result of the landing gear structures

Structure	Support span (mm)	Width at the center (mm)	Thickness at the center (mm)	Maximum flexure load (N)	Flexure extension at maximum flexure load (mm)
Landing gear 1	770	65	13	881.9	77.08
Landing gear 2	770	65	13	901.4	82.32
Average	**770**	**65**	**13**	**891.6**	**79.70**

Table 2 Properties of A-42 carbon fibers as inputs for micro-scale model

Material Property	Value
Longitudinal modulus, E_{f11} (GPa)	239.5
Transverse modulus, $E_{f22}=E_{f33}$ (GPa)	13.4
Longitudinal shear modulus, $G_{f12}=G_{f13}$ (GPa)	6.81
Transverse shear modulus, G_{f23} (GPa)	4.8
Major Poisson's ratio, $\nu_{f12}=\nu_{f13}$	0.2
Minor Poisson's ratio, ν_{f23}	0.25
Tensile strength of yarns in fiber direction, X_{fT} (GPa)	3.16
Compressive strength of yarns in fiber direction, X_{fC} (MPa)	728.8

Table 3 Properties of epoxy resin

Material Property	Value
Elastic modulus, E_m (GPa)	3.30
Elastic Poisson's ratio, ν_m	0.35
Tensile strength, X_{mT} (MPa)	60.18
Compression strength, X_{mC} (MPa)	107.37
Shear strength, S_m (MPa)	41.03

Table 4 Properties of carbon fiber/epoxy interface as inputs for micro-scale model

Material Property	Value
Interfacial shear strength, t_I (MPa)	28.12
Interface fracture energy, G_{Ic} (Jm^{-2})	12.9

Table 5 Elastic constants of the fiber yarn predicted by micro-scale analysis (V_f = 0.85)

Property	Numerical Result	Chamis equation
E_{y11}	190.25 GPa	190.90 GPa
E_{y22}	10.72 GPa	10.82 GPa
E_{y33}	10.63 GPa	10.82 GPa
G_{y12}	4.92 GPa	5.014 GPa
G_{y13}	4.3 GPa	5.014 GPa
G_{y23}	3.75 GPa	3.91 GPa
v_{y12}	0.2	0.2225
v_{y13}	0.21	0.2225
v_{y23}	0.375	0.383

Table 6 Strength values of fiber yarn predicted by micro-scale FEA model (V_f = 0.85)

Properties	X_{yT}/GPa	X_{yC}/GPa	Y_{yT}/MPa	Y_{yC}/MPa	S_{y12}/GPa	S_{y23}/MPa
Value	3.90	3.04	135.55	261.13	1.568	424.14

Table 7 Elastic constants of bi-axial braids of various braiding angles

Property	Braids of 33°	Braids of 35°	Braids of 37.2°
E_{b11}	19.93 GPa	20.17 GPa	21.25 GPa
E_{b22}	9.1 GPa	8.1 GPa	8.02 GPa
E_{b33}	9.15 GPa	9.17 GPa	9.18 GPa
G_{b12}	28.8 GPa	29.95 GPa	30.12 GPa
G_{b23}	2.4 GPa	2.6 GPa	2.8 GPa
G_{b13}	2.6 GPa	2.8 GPa	3.01 GPa
v_{b12}	0.84	0.835	0.85
v_{b23}	0.27	0.26	0.27
v_{b13}	0.13	0.13	0.13

Table 8 Strengths of bi-axial braids of various braiding angles

Property (MPa)	Braids of 33°	Braids of 35°	Braids of 37.2°
X_{bT}	364.45	363.95	350.83
X_{bC}	247.07	243.2	217.01
Y_{bT}	312.33	313.73	335.23
Y_{bC}	278.91	273.12	263.67
τ_{b12}	591.53	591.45	588.23
τ_{b23}	411.893	410	411.3
τ_{b13}	497.13	502.12	509.63